Polariton modes of spheroidal microcrystals

1998 J. Phys.: Condens. Matter 10 7869

(http://iopscience.iop.org/0953-8984/10/35/019)

J. Phys.: Condens. Matter **10** (1998) 7869–7878. Printed in the UK PII: S0953-8984(98)94539-8

Polariton modes of spheroidal microcrystals

R Ruppin†

Department of Physics, College of Humanities and Sciences, Nihon University, 3-25-40 Sakurajosui, Setagaya-ku, Tokyo 156, Japan

Received 26 May 1998

Abstract. The polariton modes of spheroidal microcrystals of dispersive materials are investigated over a wide range of spheroid sizes and eccentricities by using the T-matrix method. The method is applied to phonon-polaritons in ionic dielectric solids and to plasmon-polaritons in metallic solids. The main effects of retardation, observed when the particle size increases, are: the surface polariton peaks broaden and shift to lower frequencies; subsidiary peaks owing to higher-order surface modes appear in the spectrum. The method is applied to the interpretation of three sets of previously published experimental optical data for Ag spheroids.

1. Introduction

Our interest here is in the optical spectra of spheroidal microcrystals in frequency regions in which their dielectric constant $\varepsilon(\omega)$ is dispersive. In such regions the electromagnetic wave interacts strongly with internal degrees of freedom. The mixed excitation which consists of the oscillatory electromagnetic field clothed by the polarization induced in the medium is referred to as a polariton [1]. We will discuss the following two specific cases: (a) infrared absorption by polar ionic crystallites, where the electromagnetic field interacts with optical phonons to form phonon-polaritons; (b) optical absorption by small metal particles, where the electromagnetic field interacts with plasmons to form plasmon-polaritons.

In both cases, the spectra of small spheroids are dominated by surface polariton peaks. When the spheroid size is very small in comparison with the wavelength of the incident field, retardation effects can be neglected, and the surface mode frequencies can be obtained from electrostatic theory. In this case the induced polarization inside the spheroid is uniform, and there occur two distinct absorption peaks, the frequencies of which are given by [2]

$$\mathrm{Re}[\varepsilon(\omega_i)] = \varepsilon_m(1 - 1/n_i) \qquad i = 1, 2. \tag{1}$$

Here n_1 and n_2 are the two depolarization factors of the spheroid, and ε_m is the dielectric constant of the medium surrounding the spheroid. Let a denote the length of the semiaxis in the symmetry direction and let b denote the lengths of the other two semiaxes. The depolarization factor of a prolate spheroid for electric field along the symmetry axis is given by

$$n_1 = \frac{1 - e^2}{e^2}\left(\frac{1}{2e}\ln\frac{1+e}{1-e} - 1\right) \tag{2}$$

where the eccentricity e is given by $e = (a^2 - b^2)^{1/2}/a$.

† Present address: Soreq NRC, Yavne 81800, Israel.

0953-8984/98/357869+10$19.50

For an oblate spheroid the corresponding factor is given by

$$n_1 = \frac{1}{e^2}\left[1 - \frac{(1-e^2)^{1/2}}{e}\arcsin e\right] \tag{3}$$

where $e = (b^2 - a^2)^{1/2}/b$.

For both types of spheroids the depolarization factors for the directions perpendicular to the symmetry axis are given by

$$n_2 = (1 - n_1)/2. \tag{4}$$

While the absorption properties of very small spheroids are easily obtained from electrostatic theory, the evolvement of the spectrum with increasing spheroid size is much more difficult to calculate. The problem of the scattering of an electromagnetic wave by a spheroid of arbitrary size has been solved by Asano and Yamamoto [3], by employing a separation of variables method. Their method is very complex, and seems not to have been applied to the dispersive spheroid cases mentioned above.

Here we employ Waterman's T-matrix approach [4], which is at present one of the most powerful and widely used tools for rigorously computing light scattering by non-spherical particles. Using this method, the optical spectra of dispersive spheroids of large eccentricities will be obtained for wide ranges of spheroid sizes.

2. T-matrix method

In the framework of the T-matrix approach, the incident and scattered fields are expanded in the spherical vector wavefunctions [5]

$$\boldsymbol{M}_{\sigma mn} = \boldsymbol{\nabla} \times (\boldsymbol{r} Y_{\sigma mn}(\theta, \phi) z_n(kr)) \tag{5}$$

$$\boldsymbol{N}_{\sigma mn} = \frac{1}{k}\boldsymbol{\nabla} \times \boldsymbol{M}_{\sigma mn}. \tag{6}$$

Here the subscript σ stands for e (even) or o (odd), according to whether $\cos m\phi$ or $\sin m\phi$ is used when multiplying by the associated Legendre polynomial $P_n^m(\cos\theta)$ in order to obtain $Y_{\sigma mn}(\theta, \phi)$. $z_n(kr)$ represents a spherical Bessel or Hankel function, and $k = 2\pi/\lambda$, where λ is the wavelength. The incident and scattered fields expansions are

$$\boldsymbol{E}^i(\boldsymbol{r}) = \sum_{\nu=1}^{\infty}(a_\nu \boldsymbol{M}_\nu^1(k\boldsymbol{r}) + b_\nu \boldsymbol{N}_\nu^1(k\boldsymbol{r})) \tag{7}$$

$$\boldsymbol{E}^s(\boldsymbol{r}) = \sum_{\nu=1}^{\infty}(f_\nu \boldsymbol{M}_\nu^3(k\boldsymbol{r}) + g_\nu \boldsymbol{N}_\nu^3(k\boldsymbol{r})) \tag{8}$$

where the superscripts 1 and 3 on $\boldsymbol{M}$ and $\boldsymbol{N}$ indicate that spherical Bessel and Hankel functions, respectively, are used for the radial part. For brevity, the three indices σ, m, n have been combined to a single index ν. The unknown scattered field coefficients are related to the known incident field coefficients by the transition matrix (or T matrix) as follows

$$\begin{pmatrix} f \\ g \end{pmatrix} = T \begin{pmatrix} a \\ b \end{pmatrix}. \tag{9}$$

Waterman has developed the extended boundary condition method, from which it is found that the T matrix is given by [4, 6]

$$T = -\begin{pmatrix} K' + m_0 J' & L' + m_0 I' \\ I' + m_0 L' & J' + m_0 K' \end{pmatrix}\begin{pmatrix} K + m_0 J & L + m_0 I \\ I + m_0 L & J + m_0 K \end{pmatrix}^{-1}. \tag{10}$$

Here m_0 is the refractive index of the spheroid and the elements of the matrices are integrals over the surface of the spheroid, with

$$I_{\nu\mu} = \frac{k^2}{\pi} \int \boldsymbol{n} \cdot \boldsymbol{M}_\nu^3(k\boldsymbol{r}) \times \boldsymbol{M}_\mu^1(k'\boldsymbol{r})\, \mathrm{d}S \tag{11}$$

where $k' = m_0 k$ and $\boldsymbol{n}$ is the outward oriented surface normal. I, J, K, L differ only in the vector products appearing in the integral, which are $\boldsymbol{M}_\nu^3 \times \boldsymbol{M}_\mu^1$, $\boldsymbol{M}_\nu^3 \times \boldsymbol{N}_\mu^1$, $\boldsymbol{N}_\nu^3 \times \boldsymbol{M}_\mu^1$, and $\boldsymbol{N}_\nu^3 \times \boldsymbol{N}_\mu^1$, respectively. The primed terms in (10) are similar to the unprimed ones except that all $\boldsymbol{M}$ and $\boldsymbol{N}$ functions are of the first kind. A very useful feature of this method is that the elements of the T matrix are independent of the incident and scattered field directions, and depend only on the shape, size parameter, and refractive index of the scattering particle. Thus the T matrix need be computed only once and can then be used in calculations for any directions of light incidence and scattering. This has made it possible to derive general formulae for the optical cross sections of randomly oriented particles in terms of the matrix elements of T [7, 8]. The calculations presented here were performed with the T matrix code developed by Mishchenko [7] for the calculation of light scattering by randomly oriented particles of identical axially symmetric shape having a plane of symmetry perpendicular to the axis of rotation.

3. Phonon-polaritons in dielectric spheroids

We apply the T-matrix method to the calculation of infrared extinction spectra of diatomic ionic crystal spheroids. These are characterized by a dielectric constant of the form

$$\varepsilon(\omega) = \varepsilon_\infty + \frac{\varepsilon_0 - \varepsilon_\infty}{1 - (\omega/\omega_T)^2 - \mathrm{i}\gamma(\omega/\omega_T)} \tag{12}$$

where ω_T is the long-wavelength transverse optical phonon frequency, ε_0 and ε_∞ are the static and the high frequency dielectric constants, respectively, and γ is a damping factor. For very small spheroids, in the non-retarded limit, only two distinct peaks occur in the infrared absorption spectra, owing to the two uniform surface phonon modes, the frequencies of which are given by (1). These peaks are located in the frequency region between ω_T and ω_L (the long-wavelength longitudinal optical phonon frequency). With increasing crystallite size, retardation effects begin to contribute. By analogy with spheres, for which an analytic solution is possible, the following size effects are expected [2, 9, 10]: the peaks shift to the low frequency side, and higher-order surface modes begin to contribute, as well as bulk polaritons, which are located in the frequency region just below ω_T. Previous calculations for spheroids of this type were based on less efficient methods, and could only be implemented for a major to minor axis ratio not larger than 1.25, and semiaxes not longer than 5 μm [11].

The calculated extinction cross section of randomly oriented NaCl prolate spheroids of major to minor axis ratio of two is shown in figures 1 and 2 for various spheroid sizes. The following NaCl parameters were used in the dielectric constant [12]: $\varepsilon_0 = 5.934$, $\varepsilon_\infty = 2.328$, $\omega_T = 164\ \mathrm{cm}^{-1}$ and $\gamma = 0.02$. The spheroid size is defined in terms of the radius R of the equal volume sphere, and the extinction cross section is expressed in units of the geometric cross section, πR^2, of the equal volume sphere. For $R = 1$ μm (figure 1, (full curve)), the frequencies of the two peaks are very close to the values of 201.4 cm^{-1} and 229.7 cm^{-1} predicted by the electrostatic equation (1). For $R = 4$ μm (figure 1, (broken curve)), the surface mode peaks have broadened and shifted to lower frequencies, while a bulk mode peak near 160 cm^{-1} is observed. For larger sizes (figure 2)

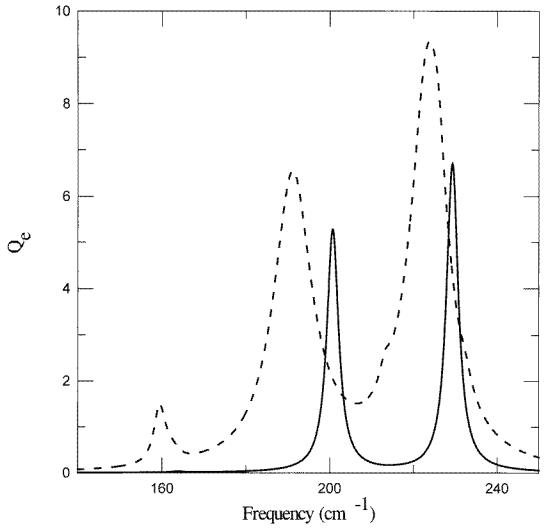

Figure 1. Extinction cross section per particle of randomly oriented NaCl prolate spheroids of axial ratio $a/b = 2$. The equal volume sphere radius is 1 μm for the full curve and 4 μm for the broken curve.

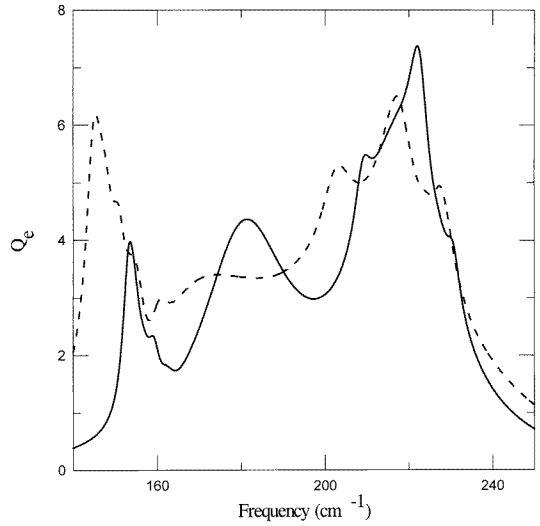

Figure 2. Extinction cross section per particle of randomly oriented NaCl prolate spheroids of axial ratio $a/b = 2$. The equal volume sphere radius is 6 μm for the full curve and 8 μm for the broken curve.

the surface polariton peaks continue to shift toward the low frequency side, and strong high order surface polariton peaks appear in the spectra. Also, the bulk mode absorption below ω_T continues to grow.

The effect of increased eccentricity is demonstrated in figure 3. The two main peaks shift in opposite directions, so that the separation between them increases with increasing major to minor axial ratio.

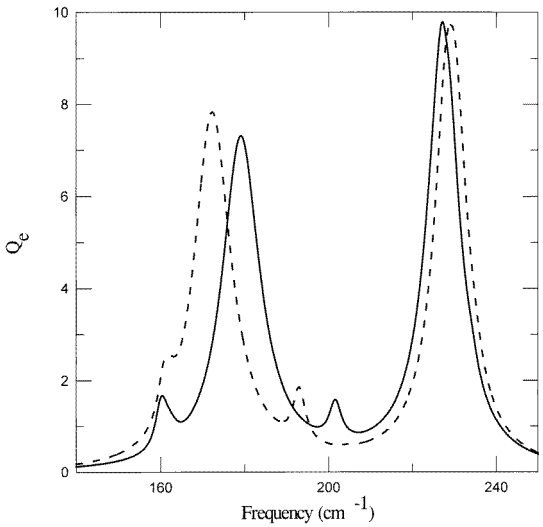

Figure 3. Extinction cross section per particle of randomly oriented NaCl prolate spheroids with equal volume sphere radius of 4 μm. The axial ratio a/b is 3 for the full curve and 4 for the broken curve.

4. Plasmon-polaritons in metallic spheroids

We calculate the extinction spectra of Ag spheroids, using for the complex dielectric constant the experimental data of Johnson and Christy [13]. The calculated extinction cross section of randomly oriented Ag oblate spheroids of major to minor axis ratio of two is shown in figures 4 and 5 for various spheroid sizes. For equal volume sphere radius $R = 5$ nm, figure 4, (full curve), the two surface plasmon peaks which appear in the spectrum are extremely close to the non-retarded values of 335.1 nm and 377.1 nm obtained from (1). For a larger size of $R = 20$ nm, figure 4, (broken curve), the peaks shift to the long-wavelength side, which is a distinct retardation effect. For even larger sizes, figure 5, the peaks broaden, owing to radiative damping, and continue to shift to the long-wavelength side. Also, a higher-order surface mode peak appears in the spectrum.

The effect of increased axial ratio, shown in figure 6, is to increase the separation between the two main peaks, owing mainly to the shift of the strongest peak towards the long-wavelength side.

5. Applications and discussion

We now present examples of applications of the theoretical method to the interpretation of experimental optical data from the literature. We have chosen three experimental cases, for which size effects are of importance, so that previous interpretations, which were based on the non-retarded theory, can be improved. Skillman and Berry [14] have produced prolate spheroids of silver by photographic development of fine-grain silver bromide embedded in gelatin. The shape and size distributions of the silver particles were determined from electron micrographs. The optical absorption was measured, and the main features were interpreted by using the electrostatic equations. In figure 7 the circles show the locations of the absorption maxima measured by Skillman and Berry [14], for five samples of small

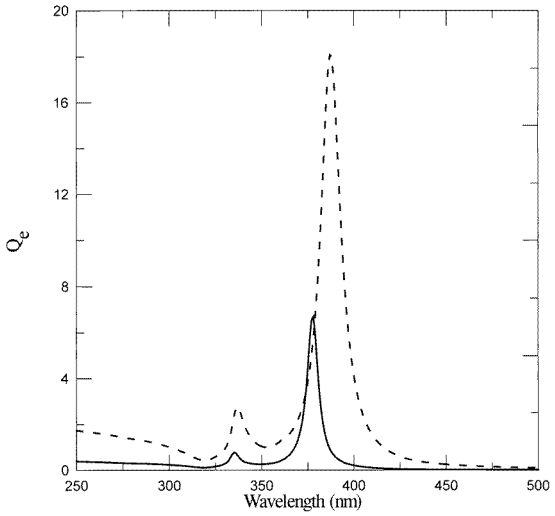

Figure 4. Extinction cross section per particle of randomly oriented Ag oblate spheroids of axial ratio $b/a = 2$. The equal volume sphere radius is 5 nm for the full curve and 20 nm for the broken curve.

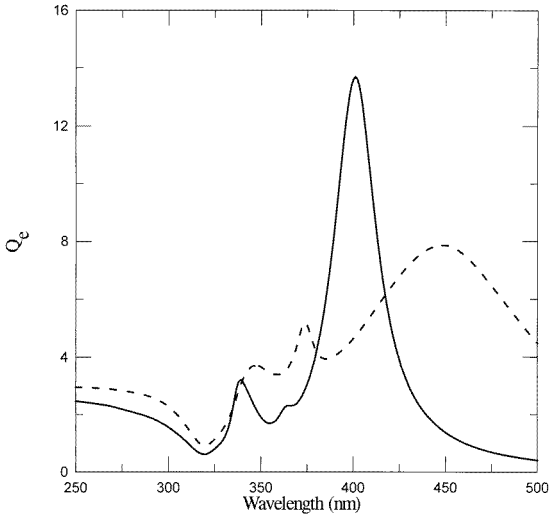

Figure 5. Extinction cross section per particle of randomly oriented Ag oblate spheroids of axial ratio $b/a = 2$. The equal volume sphere radius is 30 nm for the full curve and 50 nm for the broken curve.

axial ratio. The average axial ratios for these five samples were 0.299, 0.373, 0.380, 0.394 and 0.453. The corresponding spheroid sizes, as given by the equivalent sphere radius, were 12.2, 12.2, 14.7, 18.3 and 13.7 nm, respectively. These sizes are large enough for retardation effects to cause a shift of the absorption maxima. Since the silver prolate spheroids were embedded in gelatin, we performed the calculations with the dielectric constant of silver divided by m^2, where $m = 1.538$ is the refractive index of gelatin. The curve of figure 7 shows the location of the absorption maximum obtained from the electrostatic

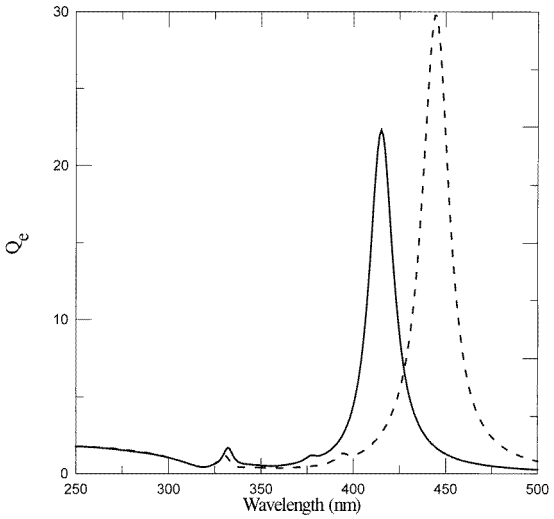

Figure 6. Extinction cross section per particle of randomly oriented Ag oblate spheroids with equal volume sphere radius of 20 nm. The axial ratio b/a is 3 for the full curve and 4 for the broken curve.

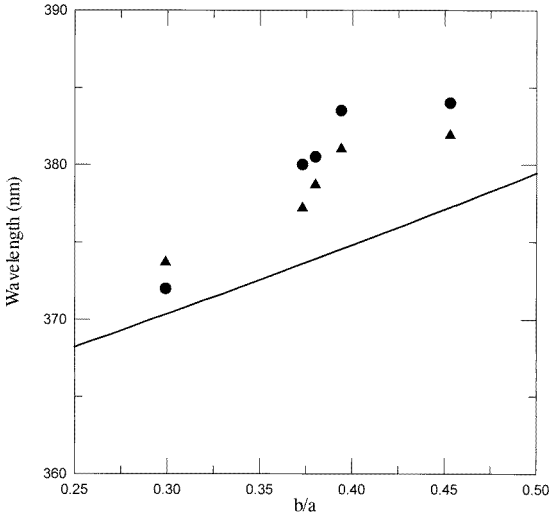

Figure 7. Wavelengths of main absorption peak of prolate Ag spheroids embedded in gelatin. The curve was calculated from the non-retarded theory. The circles represent the experimental results for five samples [14] and the triangles represent the results of the T-matrix calculations for the same samples.

equations. The triangles show the results obtained from the T-matrix calculation. They lie considerably higher than the non-retarded curve and, except for one case, are also in much better agreement with the experimental points.

Kennerly *et al* [15] have performed optical absorbance measurements on small silver oblate spheroids. Their samples were formed by evaporation of a thin film of silver onto a quartz slide. The films, approximately 5 nm thick, were electrically discontinuous. Electron

micrographs taken at normal incidence displayed islands with nearly circular cross sections. From these micrographs, the average major axis was measured to be about 60 nm.

The absorption spectra displayed two peaks, one near 340 nm and a much stronger one around about 470 nm. Since the location of the strongest peak is sensitive to the axial ratio, Kennerly *et al* [15] used it to estimate the major to minor axis ratio. However, their estimate was based on the non-retarded theory. For spheroids of major axis 60 nm, retardation already affects the spectrum. In figure 8 the theoretical dependence of the wavelength of the main peak on the axial ratio is shown, for the non-retarded case, as well as for the T-matrix retarded calculation. For the experimental value of $\lambda = 470$ nm, the T-matrix calculation yields $b/a = 0.183$, while the non-retarded theory yields $b/a = 0.170$. (The different value of 0.155, obtained by Kennerly *et al* [15] for the non-retarded case, was due to their use of different $\varepsilon(\omega)$ data.) Experimentally the oblate spheroids lay in a planar arrangement, whereas our calculations were performed for randomly oriented spheroids. This is justified by the fact that our interest here is in the frequencies of the main absorption peaks, and not in the relative intensities of the peaks (which depend on the angle of incidence).

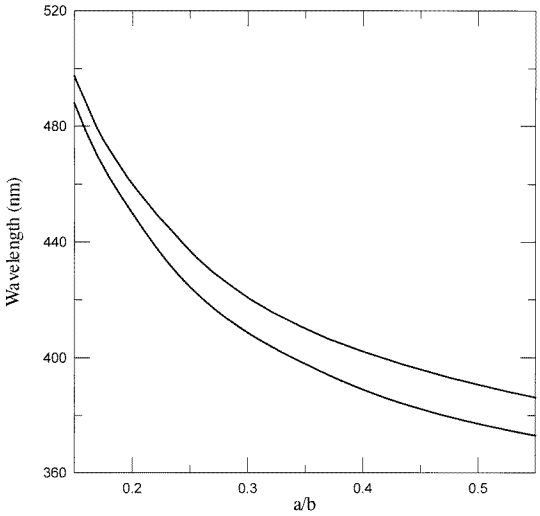

Figure 8. Dependence of the wavelength of the main absorption peak of Ag oblate spheroids on the axial ratio. The lower curve was calculated for the non-retarded case, and the upper curve was obtained from the retarded T-matrix method.

Bloemer *et al* [16] have described a growth process for fabricating silver needles over a tin oxide surface. Electron micrographs indicated that the needles were parallel, tilted about 60° from the substrate. They were about 200 nm long, and about 30 nm across. Bloemer *et al* have performed absorbance measurements in the range of 300–900 nm, and interpreted the spectra by using the electrostatic theory, modelling the needles as prolate spheroids with a major to minor axis ratio of 7:1. This model seemed to reasonably reproduce the two main peaks, which were located at about 750 and 355 nm. However, for spheroids of 200 nm size, retardation effects are so strong, that the interpretation of the spectra in terms of electrostatic theory cannot be justified. This is demonstrated by T-matrix calculations for 7:1 prolate spheroids of various sizes, the results of which are shown in figure 9. While for a semi-major axis of 5 nm the non-retarded theory is still adequate, it becomes useless for the larger spheroids, for which the main absorption peak shifts considerably to the long-wavelength

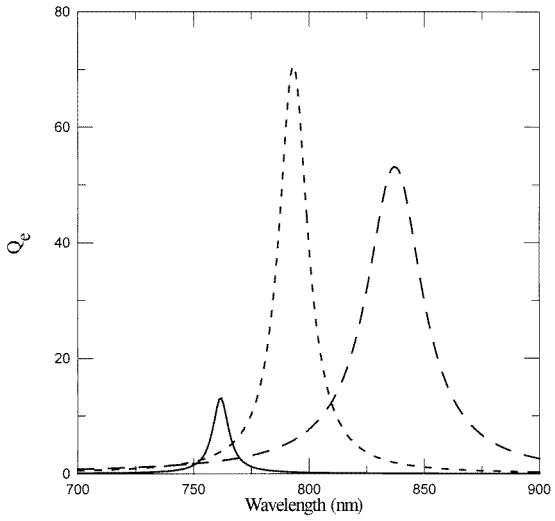

Figure 9. Main absorption peak of prolate Ag spheroids of axial ratio 7:1 and major semi-axis 5 nm for the full curve; 50 nm for the short dashed curve and 80 nm for the long dashed curve.

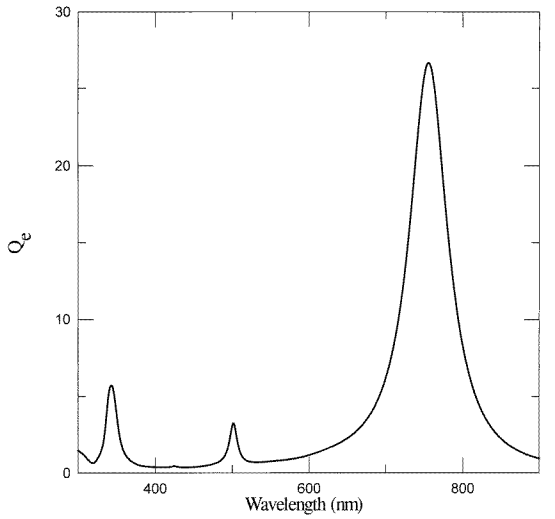

Figure 10. Extinction cross section per particle of randomly oriented Ag prolate spheroids. The lengths of the major and minor axes are 190 nm and 36 nm, respectively.

side. In order to interpret the observed spectra in terms of the retarded theory, we have to assume a smaller aspect ratio than 7:1. This is corroborated by the micrograph of the silver needles [16], which shows that there also occurred shorter and thicker needles. Representing the distribution of spheroids by an average one, having a major axis of 190 nm and a minor axis of 36 nm (so that the axial ratio is 5.3), we obtain the spectrum shown in figure 10. The locations of the two main peaks are in reasonable agreement with the experimental values. Also, there appear two secondary peaks, due to higher-order modes, at about 425 nm and 502 nm. These peaks, which are absent in the non-retarded theory, manifest themselves in

the experimental spectra of Bloemer *et al* [16] as a broad shoulder around 450 nm. All the peaks observed experimentally are much broader than the calculated peaks of figure 10. This can be attributed to the size and shape distribution which exists in the experimental sample, whereas our calculation refers to a representative, average spheroid.

In conclusion, it has been shown that the T-matrix method provides an efficient tool for the investigation of the dependence of the polariton peaks of dispersive spheroids on particle size. For both dielectric and metallic spheroids, the main effects observed when the spheroid size increases are: a shift of the surface polariton extinction peaks toward the low-frequency side; a broadening of the extinction peaks; the emergence of additional surface polariton peaks (as well as bulk polariton peaks in the case of dielectric spheroids). Calculations for Ag spheroids, for which experimental data are available, have been presented. The importance of the inclusion of retardation effects in the interpretation of the experimental data has been demonstrated.

References

[1] Mills D L and Burstein E 1974 *Rep. Prog. Phys.* **37** 817
[2] Ruppin R and Englman R 1970 *Rep. Prog. Phys.* **33** 149
[3] Asano S and Yamamoto G 1975 *Appl. Opt.* **14** 29
[4] Waterman P C 1969 *Alta Frequenza* **38** 348
[5] Morse P M and Feshbach H 1953 *Methods of Theoretical Physics* (New York: McGraw-Hill)
[6] Barber P and Yeh C 1975 *Appl. Opt.* **14** 2864
[7] Mishchenko M I 1991 *J. Opt. Soc. Am.* A **8** 871
[8] Mishchenko M I, Travis L D and Mackowski W 1996 *J. Quant. Spectrosc. Radiat. Transfer* **55** 535
[9] Fuchs R and Kliewer K L 1968 *J. Opt. Soc. Am.* **58** 319
[10] Ruppin R 1982 *Electromagnetic Surface Modes* ed A D Boardman (New York: Wiley) pp 345–98
[11] Ruppin R 1977 *Surface Sci.* **62** 206
[12] Bilz H, Genzel L and Happ M 1960 *Z. Phys.* **160** 535
[13] Johnson P B and Christy R W 1972 *Phys. Rev.* B **6** 4370
[14] Skillman D C and Berry C R 1968 *J. Chem. Phys.* **48** 3297
[15] Kennerly S W, Little J W, Warmack R J and Ferrell T L 1984 *Phys. Rev.* B **29** 2926
[16] Bloemer M J, Ferrell T L, Buncick M C and Warmack R J 1988 *Phys. Rev.* B **37** 8015